

# Gyrokinetic Simulation of Pedestal Degradation Correlated with Enhanced Magnetic Turbulence in a DIII-D ELMy H-Mode Discharge

X. Jian<sup>1,2,3</sup>, J. Chen<sup>4</sup>, C. Holland<sup>3</sup>, V. S. Chan<sup>5</sup>, X. R. Zhang<sup>6</sup>, G. Yu<sup>7</sup>, Z. Yan<sup>8</sup>

<sup>1</sup>General Atomics, P.O. Box 85608, San Diego, California 92186-5608, USA

<sup>2</sup>Institute of Plasma Physics, Chinese Academy of Sciences, Hefei, Anhui, 230031, China

<sup>3</sup>University of California, San Diego, La Jolla, California 92093-0417, USA

<sup>4</sup>University of California Los Angeles, Los Angeles, California 90095, USA

<sup>5</sup>University of Science and Technology of China, Hefei, 230026, China

<sup>6</sup>Dalian University of Technology, Dalian 116024, China

<sup>7</sup>University of California at Davis, Davis, CA 95616, USA

<sup>8</sup>University of Wisconsin-Madison, Madison, Wisconsin 53706, USA

Corresponding Author: xjian@ipp.ac.cn

**Abstract:** Gyrokinetic simulation of a dedicated pedestal density ramping-up discharge on DIII-D can reproduce the enhancement of magnetic turbulence in the pedestal, which is identified to be caused by micro-tearing modes (MTM). An increase of MTM amplitude results in higher electron thermal diffusivity, consistent with experimentally observed lower electron temperature gradient and degraded pedestal height. Gyrokinetic simulation identifies the major cause of MTM enhancement to be the increase of collisionality, which has a significant impact on the MTM intensity and is beyond the description of any (quasi-)linear theory.

## I. Introduction

ITER is designed to operate in the H-mode<sup>1</sup>, which is characterized by a transport barrier in the edge, also called the pedestal, whose strength can significantly affect the whole plasma performance<sup>2</sup>. The physics governing the pedestal strength is not fully understood yet<sup>3</sup>. Transport physics within the pedestal is believed to be vital in governing the pedestal structure because it forms the local constraint of the widely used EPED model<sup>4</sup>, which assumes the kinetic ballooning mode<sup>5,6</sup> to be the dominant transport mechanism. Moreover, the pedestal height is not always limited by MHD events<sup>7</sup>, such as in the case of the QH mode<sup>8,9</sup>, whose pedestal is argued to be limited by transport physics. Also, even for type-I ELMy H-mode<sup>10</sup>, where the EPED model applies, for most (>80%) of the time during an Edge Localized Mode (ELM) cycle, the pedestal structure is likely to be determined by transport dynamics<sup>11,12</sup>, highlighting the importance of understanding transport physics in the pedestal.

The pedestal is characterized by a strong radially sheared mean ExB flow shear<sup>8</sup>, prohibiting the existence of robust long wavelength drift-wave turbulence<sup>13</sup>. In addition to the kinetic ballooning mode, whose growth rate may surpass the ExB shearing rate, currently both the micro-tearing mode (MTM)<sup>14-17</sup> and electron temperature mode<sup>18-20</sup> (ETG) are plausible candidate instabilities in regulating the pedestal structure due to their resilience to mean flow shear. Also, both ETG and MTM fit well with the ‘transport fingerprints’<sup>21</sup> of the pedestal. Even though the ion thermal transport is close to neoclassical<sup>22</sup>, electron thermal transport is still strongly turbulence-dominated, suggesting that the underlying micro-instabilities should have the transport ‘fingerprint’ of  $\chi_i/\chi_e \ll 1$ <sup>21</sup> (here  $\chi_i$  and  $\chi_e$  are the ion and electron thermal diffusivity, respectively). Indeed, both MTM and ETG have such a transport feature. While it is still a challenge to have solid experimental evidence for the existence of ETG in the pedestal due to its small spatial scale length, significant progress has been obtained in the MTM counterpart<sup>23,24</sup>.

The MTM has been theoretically/numerically predicted to be unstable in the pedestal<sup>15,25</sup>, which is also suggested by experimental observations<sup>23,26,27</sup>. However, a comprehensive analysis of experimental data using first principles simulation to confirm MTMs to be the dominant mechanism in controlling the pedestal

gradient is still lacking. In this paper, we will show that the decrease of experimentally observed pedestal electron temperature gradient ( $\nabla T_e$ ) is correlated with the enhancement of MTM amplitude, which occurs at higher collisionality and results in an increased  $\chi_e$ . The strong dependence of the MTM amplitude on collisionality can be well reproduced in nonlinear gyrokinetic simulations, which can also qualitatively reproduce the frequency spectrum from Radial Interferometer Polarimeter (RIP)<sup>26,28</sup>. RIP measures the internal magnetic perturbation that may be representative of MTM, which can be used to estimate the induced transport flux and evaluate its experimental relevance. The combination of experiment evidence and simulation supports the significant role of MTM in the pedestal transport for the discharges under investigation. Note this discharge is not unique, we hope this work can offer a blueprint for future experiments to further confirm the role of MTM in regulating the turbulence and can provide a data point to map the instabilities that can participate under different experimental conditions.

The paper is organized as follows. Section II will show experimental observations and the MTM identification. Section III will argue the MTM to be the prominent instability in determining the pedestal gradient via a combination of gyrokinetic simulation and experimental analysis. The paper will be summarized in section IV.

## II. Experimental observation and MTM identification

Our analysis focuses on a dedicated DIII-D<sup>29</sup> discharge (#183225)<sup>30</sup> to evaluate the role of MTMs in regulating the pedestal gradient. The experimental approach is to ramp up the pedestal density, and thereby the collisionality, which is believed to be a key parameter in controlling MTM intensity, and observe the pedestal gradient/height response to the change of MTM amplitude.

The experimental dynamics are illustrated below: with the increase of pedestal density (Fig I(b)), the pedestal collisionality increases accordingly (Fig I(c)), and so does the magnetic turbulence intensity at a frequency of 200~400 kHz (Fig I(a)), and the pedestal pressure height is observed to drop drastically (Fig I(d)). The amplitude of magnetic turbulence is represented by the cross power of RIP<sup>28</sup> measured line-integrated Faraday rotation ( $\phi_{RF} = \int n_e \delta B_R dR$ ) and electron density ( $\phi_{nt} = \int n_e dR$ ) in the horizontal midplane chord along the major radius direction. Here,  $n_e$  is the electron density and  $\delta B_R$  is the radial/horizontal magnetic perturbation. The magnetic turbulence is inferred to exist in the pedestal region since it is correlated with the pedestal evolution as indicated by the periodic synchronization between the magnetic turbulence amplitude and the  $D_\alpha$  signal (Fig I(e) and I(f)) transiently emitted when ELMs occur. Magnetic turbulence is weakest after the pedestal collapses after the ELM and becomes stronger with advancing time until the next ELM event<sup>26</sup>. Such an observation does not seem to apply to the fluctuations <100kHz, suggesting it is unlikely to be relevant to the pedestal behavior and is out of interest in this paper. Even though, more efforts are also deserved to be invested to such a part in the future.

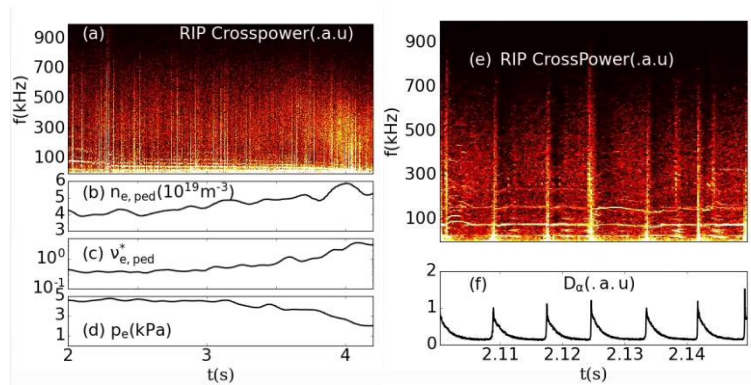


Figure I. (a) Crosspower of RIP density and Faraday angle measurement in the midplane chord.

Temporal evolution of (b) pedestal density, (c) pedestal collisionality, and (d) pedestal electron pressure.

Zoom view of the temporal dynamics of (e) RIP crosspower and (f)  $D_\alpha$  signal.

To identify the nature of the magnetic turbulence, its dispersion relation is examined. Take the time slice at  $t=3800$  ms as an example, with the beam emission spectroscopy (BES) system<sup>31,32</sup>, whose array covers the whole pedestal region for this discharge (Fig 2(a)), the coherence and cross phase between two radially aligned channels in the pedestal can be obtained (Fig 2(b) and 2(c)). The phase velocity of the mode in the laboratory frame can thus be estimated to be  $\sim 60$  km/s as denoted by  $v_{BES}$  in Fig 2(d) marked with a purple dashed line (the purple shadow box represents the uncertainty). The inferred mode phase velocity  $v_{BES}$  matches well with the peak value of  $v_{tot}$ , which is the sum of electron diamagnetic velocity ( $v_{*pe}$ ) and ExB velocity ( $v_{Er}$ ), consistent with the theoretical expectation of the MTM dispersion relation<sup>15,33</sup> and suggesting the mode to be excited around the peak gradient region in the pedestal. Also, the coherence peaks at a frequency of 260~300 kHz (Fig 2(b)), consistent with the frequency spectrum of magnetic turbulence measured by RIP (Fig. 1(a)). The destabilization of MTM in the pedestal is also supported by both linear and nonlinear gyrokinetic simulations, as will be discussed in the next section, which argues the MTM to be the prominent mechanism regulating the pedestal (electron temperature) gradient.

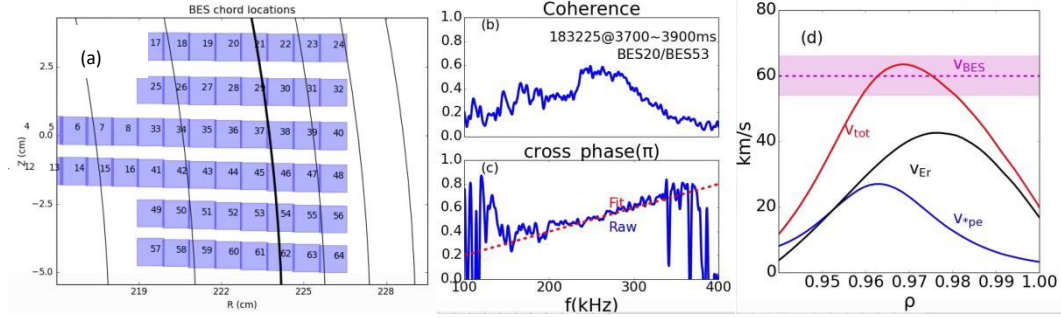


Figure 2. For DIII-D shot #183225@3800ms. (a) BES layout; (b) coherence and (c) cross phase between channel 20 and 53; (d) comparison between the phase velocity inferred from BES ( $v_{BES}$ ) and the sum ( $v_{tot}$ ) of electron diamagnetic ( $v_{*pe}$ ) and ExB velocity ( $v_{Er}$ )

### III. Gyrokinetic simulation

Section II has identified the mode as MTM based on its dispersion relation. Experimentally it is observed that both the degradation of electron pressure and the enhancement of electron thermal diffusivity are correlated with the enhancement of MTM amplitude. In the following sections, we will pick time slices of 2700ms and 3800ms to represent the early phase (low MTM amplitude) and later phase (high MTM amplitude), respectively, for comparative analysis. The goal is to quantify the role of MTMs in regulating the pedestal gradient. More specifically, we want to answer the following questions:

- 1) Whether the experimental identified MTM can be reproduced by gyrokinetic modeling
- 2) How big a role does MTM play in the pedestal transport
- 3) What controls the MTM amplitude in its temporal dynamics

It will be shown in this section that the experimentally identified MTM can be reproduced by gyrokinetic modeling, specifically, the MTM is linearly unstable for both phases. The RIP-measured magnetic turbulence frequency spectrum can be qualitatively reproduced by nonlinear gyrokinetic simulations, highlighting the relevance of MTM predicted by the gyrokinetic modeling to the experimentally observed magnetic turbulence. Here gyrokinetic simulations are performed in the (local) flux-tube mode with the CGYRO<sup>34</sup> code, which is a first-principles tool optimized for studying electromagnetic instabilities. The induced flux  $\chi_e$  obtained

from nonlinear simulations also predicts the MMTM-induced flux to be experimentally relevant. Partly because of the unavoidable uncertainties of input quantities (eg, kinetic gradients  $\nabla T_e$ ) for nonlinear simulation, estimation of the  $\chi_e$  ratio between the two phases is also performed with the input directly coming from the RIP-measurement magnetic fluctuation intensity. It suggests  $\chi_e$  to be  $\sim 40\%$  higher in the later phase, consistent with the power balance analysis (which predicts a 50% increase of  $\chi_e$  in the later phase<sup>35</sup>), indicating the significant (or even dominant) role of MTM in regulating the pedestal gradient. Furthermore, dedicated analysis suggests that the enhanced collisionality is the dominant parameter amplifying the MTM intensity in the later phase. It is noted that in the pedestal region, a global code is better at capturing the comprehensive physical effect in principle. However, in practice, global codes sometimes encounter numerical issues due to the strong profile variation across the pedestal<sup>36</sup>. Here a flux-tube approach is employed, since it is more robust in the numerical algorithm, though at some cost of accuracy, and allows us to do more exploration of parameter space as will be shown in this paper.

### III.I Verify the experimentally observed MTM to be produced by gyrokinetic modeling

We will go step-by-step to show that CGYRO can well reproduce the RIP-measured magnetic turbulence. It will be shown that 1) MTM is linearly unstable for both phases from linear CGYRO simulation; 2) MTM persists as the dominant mode in the nonlinear phase; and 3) the nonlinear CGYRO-predicted MTM frequency spectrum can qualitatively match the RIP measurement.

#### Step I. Linear CGYRO simulation to verify the MTM to be unstable in both phases

Motivated by experimental observations that the MTM is excited in the peak gradient region of the pedestal (Fig 2(c)), linear calculations for both time slices are performed at  $\rho = 0.96$ , where  $-dT_e/dr$  peaks (Fig 3(a)). More background parameters are summarized in Table I. Here the normalized temperature

gradient  $a/L_{Te} = -a \nabla T_e / T_e$ ,  $a/L_{Ti} = -a \nabla T_i / T_i$ , the ExB shearing rate  $\gamma_E = \frac{a}{c_s} \frac{r}{q} \frac{\partial \omega_0}{\partial r}$  where  $\omega_0$  is

the toroidal rotation frequency induced by the radial electric field  $E_r$ .<sup>37</sup> Also,  $\beta_{e,unit} = 8\pi n_e T_e / B_{unit}^2$  where  $B_{unit}$  is the local effective field strength<sup>38</sup>, and  $\nu_e$  is the collisional frequency defined as  $\nu_e =$

$\frac{a}{c_s} \frac{\sqrt{2}\pi e^4 n_e}{m_e^{0.5} T_e^{1.5}} \ln \Lambda$ , where  $c_s$ ,  $m_e$  and  $e$  are the ion sound speed, electron mass and electron charge,

respectively and  $\ln \Lambda$  is the Coulomb logarithm.

With the up-down asymmetry of the shaping effect retained<sup>39</sup>, linear CGYRO simulation results are shown in Fig 3. MTM is shown to be robustly unstable with nominal experimental parameters. The mode is identified to be MTM for three reasons: 1) its frequency aligns well with the electron diamagnetic frequency  $\omega_{*pe}(c_s/a) = -k_y \rho_s (a/L_{Te} + a/L_{ne})$  (Fig 3(c)), here the minus sign denotes the electron diamagnetic direction; 2)  $\Phi$  is odd and  $A_{||}$  is even in its eigenfunction structure (though not in a perfect way probably due to shaping effect); 3) a quasi-linear calculation indicates the mode is most efficient in inducing electron thermal transport via magnetic fluttering (not shown here). It is worthwhile to mention that the stable gap ( $0.05 > k_y \rho_s > 0.03$ ) in the case of 3800ms (Fig 3(d)) is caused by the branch transition of MTM, eg, the eigenfunction of  $k_y \rho_s = 0.02$  and  $k_y \rho_s = 0.08$  are qualitatively different, while why one MTM branch is suitable to exist in one certain  $k_y \rho_s$  range and the other one favors another  $k_y \rho_s$  range remains to be investigated.

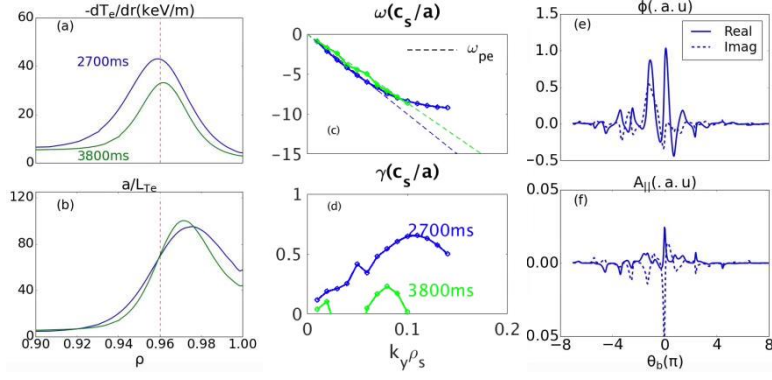


Figure 3. Comparison of (a)  $-dT_e/dr$ , (b)  $a/L_{Te}$ , (c) mode frequency  $\omega$  and (d) growth rate  $\gamma$  between the two time slices. The eigenfunction of (e)  $\phi$  and (f)  $A_{||}$  of  $k_y \rho_s = 0.06$  for time slice of 2700ms

Table I. Experimental parameters of  $\rho_{tor}=0.96$  (183225@2700ms&3800ms)

$r_{min}/a$	$a/L_{Te}$	$a/L_{Ti}$	$a/L_{ne}$	$a/L_{ni}$
0.973/0.974	69.1/70.1	13.6/5.95	31.7/15.4	30.1/11.7
s	q	$\beta_{E,unit}$	$\gamma_E(c_s/a)$	$v_e(c_s/a)$
0.74/2.62	5.11/5.10	1.79e-4/2.1e-4	1.00/1.00	1.14/2.97

## Step II. Verify the persistence of MTM turbulence in the nonlinear phase

It has been reported that the MTM can be eliminated in the nonlinear phase under some conditions<sup>40</sup> (eg. via nonlinear interaction with subdominant drift wave turbulence) even though it is linearly unstable, therefore, it is necessary to verify the persistence of MTM and test if MTM is still important/dominant in the nonlinear phase. The nonlinear simulation is performed for both time slices with resolution parameters shown in Table II. Here,  $\Delta k_x \rho_s$  and  $\Delta k_y \rho_s$  are the interval (also minimum value) of the radial and bi-normal wave number, which are determined by the simulation box size,  $k_{x,max} \rho_s$  and  $k_{y,max} \rho_s$  are the maximum resolved  $k_x \rho_s$  and  $k_y \rho_s$ , and  $N_\theta$  is the number of poloidal angle gridpoints.

With experimental  $E_r$  shear turned on, resultant temporal dynamics of fluxes are shown in Fig 4, in which the well-saturated state and sensible flux spectrum suggest the nonlinear run to be reasonable. Note that the reason that the  $E_r$  shear is turned on is just to try to mimic the experimental conditions as closely as possible, we have dedicatedly tested the role of  $E_r$  shear, which shows little effect on the predicted flux even though the  $E_r$  shearing rate is larger than the maximum growth rate(not shown here). In addition, a box convergence check is also performed, and similar results are observed, further suggesting the nonlinear runs to be valid.

Table II. Resolution parameters in CGYRO nonlinear simulation

Case	$\Delta k_x \rho_s$	$k_{x,max} \rho_s$	$\Delta k_y \rho_s$	$k_{y,max} \rho_s$	$N_\theta$
2700ms	0.023	2.96	0.01	0.23	96
3800ms	0.082	5.18	0.01	0.23	96

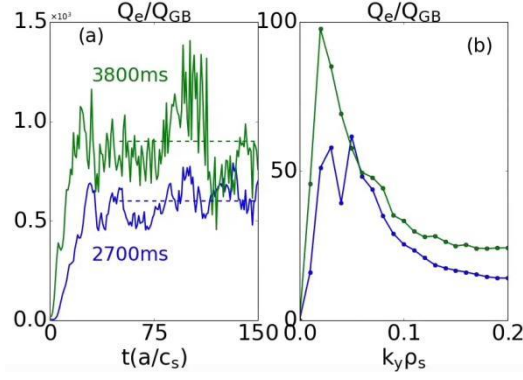


Fig 4 Comparison of (a) temporal flux dynamics, and (b) flux spectrum of the two slices. Comparison of fluctuation amplitude of the two slices in the saturated phase, averaged over 50~150  $a/c_s$

To verify that the MTM persists in the nonlinear phase, a Fourier transform of  $A_{||}$  from temporal dynamics to frequency space is performed in the nonlinear phase<sup>41</sup>, and the nonlinear dispersion relation can be thus obtained (Fig 5). As can be seen, for every  $k_y \rho_s$ , the nonlinear mode intensity peaks at the MTM linear frequency (denoted by the black dashed line), suggesting that the MTM persists and dominates in the nonlinear phase for both time slices.

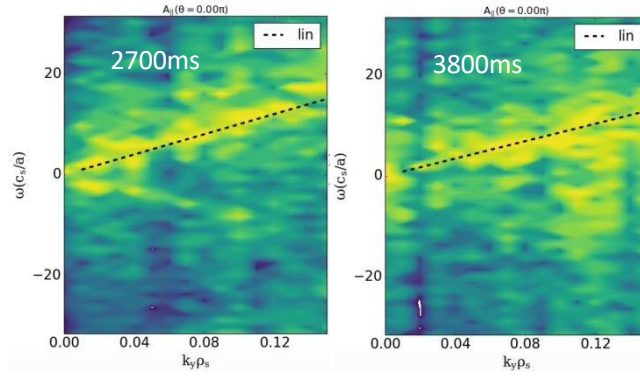


Figure 5. Comparison of the dispersion relation of the linear (black dashed line) and nonlinear simulation (contour plot) for both 2700 ms (left panel) and 3800 ms (right panel). Here the positive sign represents the electron diamagnetic direction

### Step III. Comparison of the magnetic spectrum between RIP and nonlinear CGYRO

Although we have demonstrated the persistence of MTM in the nonlinear phase, the relevance between the MTM that CGYRO simulated and that observed in RIP requires verification. One way to link is to compare the RIP-measured magnetic frequency spectrum with that of the nonlinear CGYRO prediction, which is done in this section.

RIP measures the line-averaged radial magnetic fluctuation amplitude ( $\delta \bar{B}_r$ ) defined as<sup>27</sup>

$$\delta \bar{B}_r \approx \delta \bar{B}_R = \sqrt{\frac{\int n_e \delta B_R dR}{\int n_e dR}} \quad (IV.1)$$

Here  $\int dR$  means line integral along the horizontal direction in the major radius(R).  $\delta \bar{B}_r$  thus has the form of  $\delta B_R \Delta R$ , with  $\delta B_R$  the radial magnetic perturbation and  $\Delta R$  of its radial width. Assuming  $\Delta R \sim \Delta Z \sim 1/k_y$ , here  $k_y$  is the poloidal wave number and  $\Delta Z$  is the poloidal wavelength, we have

$$\delta B_R \Delta R \sim \delta B_R / k_y \sim A_{||} \quad (IV.2)$$

Therefore, it makes sense to compare the frequency spectrum of  $\delta \bar{B}_r$  from RIP with  $A_{||}$  from nonlinear CGYRO with the assumption that  $\delta \bar{B}_r$  represents the strength of local magnetic perturbation.

Here we do not aim to compare the absolute amplitude between RIP and CGYRO output, but a qualitative comparison is doable (the amplitude of  $A_{||}$  in the CGYRO output is multiplied by the same scaling factor for the two phases for better visualization). Results are shown in Fig 6, clearly indicating that the nonlinear CGYRO simulation can reasonably well reproduce the magnetic frequency spectrum shape in both phases, suggesting the strong relevance between the CGYRO simulated MTM and experimentally observed magnetic turbulence. Here the frequency  $f$  in the x-axis is mapped from the  $k_y \rho_s$  in the nonlinear CGYRO simulation with  $f \sim k_y (v_{\text{phase}} + v_{\text{ExB}})$ , while  $v_{\text{phase}}$  and  $v_{\text{ExB}}$  are the phase velocity and ExB velocities, respectively.

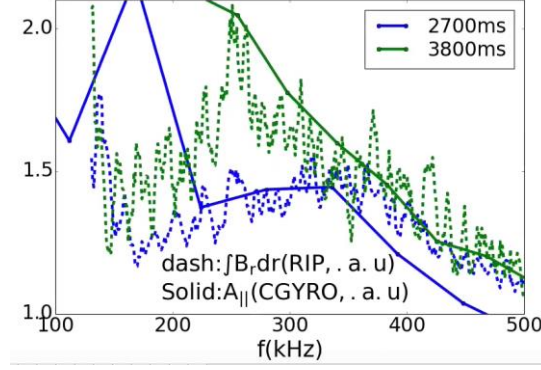


Figure 6. Frequency spectrum comparison between  $\delta \bar{B}_r$  from RIP and  $A_{||}$  from nonlinear CGYRO

### III.I Quantify the role of MTM in pedestal transport

To quantify the role of MTM in pedestal transport, two approaches are employed here. One is to directly compare the experimental power balance value to the nonlinear CGYRO prediction. Such an approach is justified by the demonstration of nonlinear CGYRO predicted MTM to be experimentally relevant in Section III.I. Since the CGYRO predicted fluxes can be affected by uncertainties in the input parameters, which are challenging to quantify in the pedestal, an alternative/supplementary approach is to compare the  $\chi_{e,3800ms}/\chi_{e,2700ms}$  ratio between the power balance value and the one inferred directly from the RIP  $\delta \bar{B}_r$ . It will be shown in this section that 1) the nonlinear CGYRO predicted fluxes based on nominal parameters are qualitatively consistent with the experiment, 2) direct estimation from RIP-measured  $\delta \bar{B}_r$  gives  $\chi_{e,3800ms}/\chi_{e,2700ms} \sim 1.4$  while experimental value is  $\sim 1.5$ . Both results support the key role of MTM in pedestal transport.

#### Approach I. Direct comparison of CGYRO predicted flux versus power balance value

With the nominal parameters as input, flux comparison between nonlinear CGYRO prediction and power balance value is shown in Table III. The CGYRO prediction is higher than the experimental value, which is reasonable since CGYRO predicts that a broad range of  $k_y \rho_s$  (0.01~0.24) can contribute to the induced flux, whereas experimentally the contributing  $k_y \rho_s$  spectrum is narrower. As shown in Fig. 6, the high  $B_r$  intensity predicted by CGYRO at low  $k_y \rho_s$  (eg.  $k_y \rho_s < 0.05$  for low pedestal case, roughly corresponds to  $f < 200$  kHz in Fig. 6) is significantly diminished in the RIP measurement. This is understandable since CGYRO is a local code that assumes a rational surface exists for every  $k_y \rho_s$ , but it is not always so under real experiments. A recent study utilizing global simulations<sup>42</sup> suggests that the mode can be excited only when the peak gradient region is sufficiently close to the corresponding rational surface. Such a condition is more difficult to satisfy for lower  $k_y \rho_s$ , consistent with the observation that the spectra match is poorer for the modes of lower  $k_y \rho_s$  (also thus of lower frequency, eg  $f < 200$  kHz) in Fig. 6. On top of this, if we then only consider the flux which is contributed by modes that are observed in experiments (eg.  $k_y \rho_s > 0.05$ ), then the flux is clearly decreased but still higher than the experimental value, however, it

makes the flux match feasible, eg, a 30% reduction of  $a/L_{Te}$  (which is marginally within experimental uncertainties) gives a reasonable agreement with power balance value (Table III). Furthermore, the profile curvature, which is the second radial derivative of the kinetic profiles and is drastic in the pedestal region, can suppress the transport flux to some extent, eg, simulation with profile curvature can reduce the flux by  $\sim 20\%$  based on nominal parameters. Therefore, the requirement for the  $a/L_{Te}$  reduction for flux match can be further relaxed if the profile curvature is considered. It should be noted that since the MTM has a characteristic size of  $k_y \rho_s \sim 0.06$  (corresponds to the peak of magnetic spectrum in Fig. 6 for the early phase, see Figure 4(b)), the corresponding radial width is quite large and therefore non-local effects on governing parameters (eg, collisionality and magnetic shear) might be important, especially considering it is located in the pedestal, where profile variation is strong. Both the uncertainties and global effect are difficult to quantify, so we do not pursue to accurately match the flux following this approach, even though it is doable with some assumptions. The qualitative comparison provides a sense that the CGYRO predicted flux is experimentally relevant and the discrepancy between the power balance value and CGYRO prediction is understandable.

Table III Comparison of CGYRO predicted electron energy flux versus experimental power balance value

Gyrobohm normalized electron thermal flux	CGYRO Simulation (fully $k_y \rho_s$ )	CGYRO Simulation ( $k_y \rho_s > 0.05$ )
2700ms (PB value: 150)	Nominal $a/L_{Te}$ : 630 -20% $a/L_{Te}$ : 390 -30% $a/L_{Te}$ : 250	Nominal $a/L_{Te}$ : 400 -20% $a/L_{Te}$ : 250 -30% $a/L_{Te}$ : 140
3800ms(PB value: 300)	900	538

### Approach II. compare the $\chi_{e,3800ms}/\chi_{e,2700ms}$ between PB value and inferred value from RIP $\delta \bar{B}_r$

Starting directly from the RIP measured  $\delta \bar{B}_r$ , and assuming it represents the local magnetic perturbation, it can be inferred that the electron thermal diffusivity ( $\chi_{e,EM}$ ) contributed by MTM induced magnetic fluttering is higher for the later phase. Quantitatively, we use the following expression to relate the diffusivity  $\chi_{e,EM}$  to the magnetic fluctuation intensity  $\bar{B}_r$  (See Appendix A),

$$\chi_{e,EM} \sim \frac{Q_e}{n_e \nabla T_e} \sim \frac{1}{n_e} \frac{T_e}{\nabla T_e} \left\langle \frac{\bar{B}_r^2}{k_y} \right\rangle \quad (IV.3)$$

While  $\frac{T_e}{\nabla T_e}$  is almost the same between the two phases (Fig 3(b) at the mode peaking location

( $\rho=0.96$ ),  $n_e$  and  $B_r^2/k_y$  is  $\sim 10\%$  (at  $\rho=0.96$ ) and  $\sim 50\%$  higher, respectively (averaged over frequency of 150~400kHz where clear coherence is observed (Fig2.(b))). This results in the estimated  $\chi_{e,EM} \sim 40\%$  higher in the later phase, which is close to the power balance value with  $\chi_e \sim 50\%$  higher in the later phase.

### III.3 Evaluating the collisionality effect on the MTM

Fig 3(d) shows that the growth rate is lower while the resultant flux is higher ( Fig 4(a)) in the later phase, which has higher collisionality. This section aims at understanding the role of collisionality in the linear growth rate and nonlinear flux of MTM, hence explaining the observed experimental temporal dynamics.

#### Q.I: Why the growth rate is lower in the later phase

A detailed comparison of the parameters between the two phases (Table I) reveals that in addition to the more than doubling in collisionality, the magnetic shear also exhibits a drastic rise (Fig 7). This is reasonable since the combination of lower pedestal pressure and higher collisionality in the later phase lowers the bootstrap current, which makes it more difficult to reverse/flatten the  $q$  profile at the pedestal; higher magnetic shear is thus obtained.

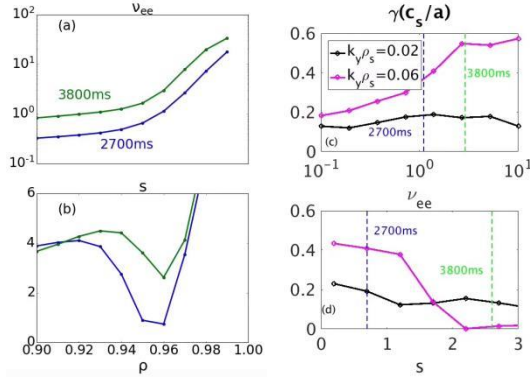


Figure 7. Comparison of collisionality (a) and magnetic shear (b) profile across the pedestal region; dependence of the growth rate of the two representative  $k_y \rho_s$  values on (c) collisionality and (d) magnetic shear

By scanning collisionality and magnetic shear with background parameters coming from the early phase, it is found that while the higher collisionality can increase the growth rate (Fig 4(c)), the higher magnetic shear can enter linearly to significantly suppress the MTM<sup>43</sup> (especially for  $k_y \rho_s = 0.06$  (Fig 7(d))) and thus leads to a lower growth rate in the later phase. However, this does not infer that the induced flux is lower.

#### Q.2: Why the nonlinear flux is higher in the later phase despite of lower growth rate

The higher flux in the later phase is partly attributed to its higher saturation amplitude (Fig. 8), which is consistent with experiments indicating that the later phase has a greater magnetic fluctuation intensity ( Fig. 6). However, the fact that higher fluctuation intensity comes from lower growth rate suggests that quasi-linear theory<sup>44</sup> cannot be applied to predict the MTM turbulent induced flux. Also, finite flux is generated at the linearly stable  $k_y \rho_s$  domain (eg  $k_y \rho_s > 0.1$  for the later phase), which further substantiates the inadequacy of quasi-linear theory/model in describing the nonlinear MTM dynamics.

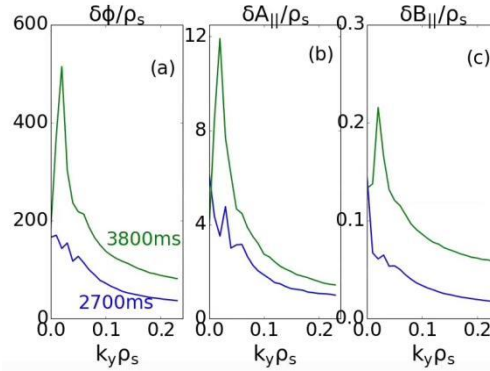


Figure 8 (a) fluctuation electrostatic potential  $\frac{1}{\rho_s} \frac{\delta\phi}{eT_e}$ ; (b) magnetic vector potential  $\frac{c_s}{\rho_s} \frac{e\delta A_{||}}{T_e}$  and (c) parallel

$$\text{magnetic field strength } \frac{1}{\rho_s} \frac{\delta B_{||}}{B_{unit}}$$

To further verify/understand both the linear and nonlinear results in both phases, we try quantifying the role of collisionality and magnetic shear on the flux (Fig. 9). The approach is to start with the background parameters coming from the early phase, and by changing the collisionality and magnetic shear separately to the values of later phase, we use CGYRO simulation to evaluate their roles on both the linear growth rate and nonlinear flux. While visually the magnetic shear can significantly suppress the linear growth rate and the collisionality enhancement of growth rate is limited (Fig 9 left panel), the flux change behavior

shows an opposite trend (Fig 9 right panel), namely, the magnetic shear induced flux reduction is limited (40% decrease in total) while collisionality enhancement of the flux is drastic (3 times higher in total). Fig 9(b) is consistent with previous observations and highlights the significant role of collisionality in flux enhancement, which is well beyond what the quasi-linear theory can predict, and illustrates the varying impact of collisionality and magnetic shear on different wavenumbers.

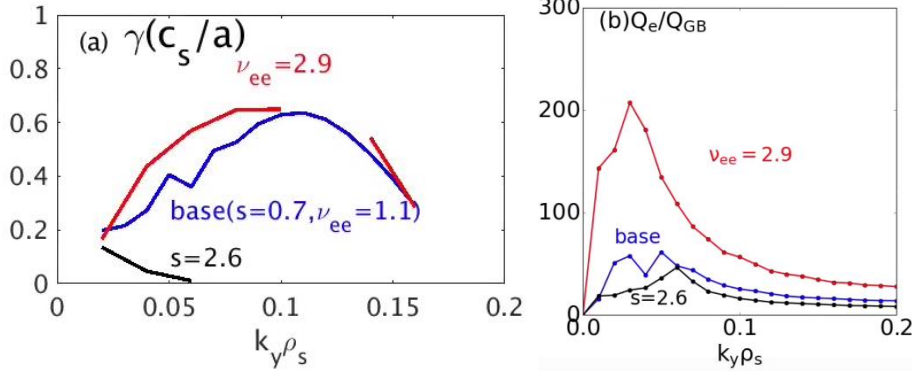


Figure 9. Spectrum of linear growth rate(a) and electron energy flux spectrum(b). Blue line: base case coming from the early phase; red: collisionality change only; black: magnetic shear change only

The key finding of our nonlinear study is that the higher flux and fluctuation level in the later phase can be attributed to its higher collisionality. The collisionality induced nonlinear flux enhancement is far larger than the quasi-linear theory can describe. More generally, the quasi-linear theory is not expected to describe the nonlinear dynamics of MTM, which might be a challenge for developing reduced models accounting for MTM induced transport.

#### IV. Conclusion

In this paper, we have carefully examined the role of magnetic turbulence, which is identified to be an MTM, in pedestal transport in a DIII-D ELMy H-mode plasma. The conclusion is that MTM is likely to play a significant role in regulating the pedestal kinetic profiles based on the following rationales:

1. Linear CGYRO calculations based on nominal experimental parameters predict the MTM to be unstable in the pedestal peak gradient region;
2. Nonlinear CGYRO predicted frequency spectrum of magnetic turbulence is qualitatively consistent with experiments; this is essential to the successful validation of nonlinear CGYRO simulation, which predicts the MTM-induced flux to be experimentally relevant;
3. Direct estimation of magnetic fluttering induced flux from RIP measured magnetic turbulence suggests higher electron thermal diffusivity in the later phase, consistent with experiments.

Combining the 3 points above, we arrive at a coherent picture. Due to the enhanced collisionality in the later phase (caused by the density increase), the saturated level of MTM becomes higher (reproduced by CGYRO and validated via RIP), which causes higher electron thermal diffusivity. Its level is within the range obtained from experimental power balance analysis and causes the pedestal gradient to drop, which explains the observed pedestal degradation. It should be noted that here 1) while we stress the dominant role of MTM in doing the thermal transport in the pedestal region, we do not mean to rule out the existence of other possible candidate transport mechanisms, like the dissipative trapped electron mode(DTEM), whose strength is also expected to increase with collisionality. However, we do not think the DTEM is taking the leading role in the pedestal transport that we studied here, since such a mode is efficient in driving both particle and electron thermal transport while experimentally no saturation of density channel is observed and

electron temperature is clearly clamped, suggesting the dominant underlying mode should drive more electron thermal flux than its particle counterpart, and MTM fits better in such a transport fingerprint. But anyway, more work should be done to figure out additional candidates and their roles in the pedestal transport; 2) in the comparison between experimental energy flux and CGYRO prediction, a flux-tube approach is employed, which overpredicts the flux. A global treatment should be used to resolve the discrepancies and is left for future work.

As an interesting theoretical observation, a comparison between linear and nonlinear CGYRO calculations reveals that

1. the flux enhancement by collisionality is beyond quasi-linear prediction;
2. Non-negligible flux is contributed by modes of  $k_y \rho_s$  which are linearly stable.

The two observations suggest that nonlinear MTM dynamics are unlikely to be described by (quasi-)linear estimations, raising a challenge for developing reduced models for MTM. To proceed, it is required to dig more into the saturation physics of the MTM. And here we raised two observations, as shown above, that future theories should be able to explain when they are proposed.

### Appendix I : Derivation of expression for $\chi_{e,EM}$

From the continue equation, we have

$$\frac{\partial \tilde{p}_e}{\partial t} \sim \tilde{V} \cdot \nabla p_e \quad (\text{A.1})$$

Here,  $\tilde{p}_e$  is the perturbed electron pressure, and  $\tilde{V}$  is expressed in the form of  $v_{e,\parallel} \tilde{B}_r$ , where  $v_{e,\parallel}$  and  $\tilde{B}_r$  is electron parallel velocity and radial perturbed magnetic field, respectively. Performing Fourier transformation to the frequency space will lead to

$$\omega \tilde{p}_e \sim v_{e,\parallel} \tilde{B}_r \nabla p_e \quad (\text{A.2})$$

The dispersion relation for the MTM has

$$\omega \sim k_y \nabla p_e \quad (\text{A.3})$$

Combining Eqn(A.2) and (A.3) gives

$$\tilde{p}_e \sim \frac{v_{e,\parallel} \tilde{B}_r}{k_y} \quad (\text{A.4})$$

The electron thermal flux induced by magnetic fluttering takes on the form

$$Q_{e,EM} \sim \langle \tilde{Q}_{e,\parallel} \tilde{B}_r \rangle \sim v_{e,\parallel} \langle \tilde{p}_e \tilde{B}_r \rangle \quad (\text{A.5})$$

The expression  $\tilde{Q}_{e,\parallel} \sim v_{e,\parallel} \tilde{p}_e$  is used in the above equation. Substituting Eqn(A.4) to Eqn(A.5) will give

$$Q_{e,EM} \sim v_{e,\parallel} \langle \tilde{p}_e \tilde{B}_r \rangle \sim v_{e,\parallel}^2 \langle \frac{\tilde{B}_r^2}{k_y} \rangle \sim v_{th,e}^2 \langle \frac{\tilde{B}_r^2}{k_y} \rangle \sim T_e \langle \frac{\tilde{B}_r^2}{k_y} \rangle \quad (\text{A.6})$$

The diffusivity  $\chi_{e,EM}$  is related to  $Q_e$

$$\chi_{e,EM} \sim \frac{Q_e}{n_e \nabla T_e} \quad (\text{A.7})$$

Substitute Eqn(A.6) to Eqn(A.7) gives

$$\chi_{e,EM} \sim \frac{Q_{e,EM}}{n_e \nabla T_e} \sim \frac{1}{n_e} \frac{T_e}{\nabla T_e} \langle \frac{\tilde{B}_r^2}{k_y} \rangle \quad (\text{A.8})$$

### Acknowledgment

This material is based upon work supported by the U.S. Department of Energy, Office of Fusion Energy Sciences, under Award Nos. DE-SC0018287, DE-SC0017992, DE-SC0023500, DE-FG02-95ER54309, DE-SC0019004, DE-FG02-08ER54999 and DE-FC02-04ER54698. This research used

resources of the National Energy Research Scientific Computing Center (NERSC); a U.S. Department of Energy Office of Science User Facility operated under Contract No. DEAC02-05CH11231 using NERSC award ERCAP0020598. We also appreciate the anonymous referees for many good suggestions.

**Disclaimer:** This report was prepared as an account of work sponsored by an agency of the United States Government. Neither the United States Government nor any agency thereof, nor any of their employees, makes any warranty, express or implied, or assumes any legal liability or responsibility for the accuracy, completeness, or usefulness of any information, apparatus, product, or process disclosed, or represents that its use would not infringe privately owned rights. Reference herein to any specific commercial product, process, or service by trade name, trademark, manufacturer, or otherwise does not necessarily constitute or imply its endorsement, recommendation, or favoring by the United States Government or any agency thereof. The views and opinions of authors expressed herein do not necessarily state or reflect those of the United States Government or any agency thereof.

## References

1. F. Wagner, G. Becker, K. Behringer, D. Campbell, A. Eberhagen, W. Engelhardt, G. Fussmann, O. Gehre, J. Gernhardt and G. v. Gierke, *Physical Review Letters* **49** (19), 1408 (1982).
2. J. E. Kinsey, G. M. Staebler, J. Candy, R. E. Waltz and R. V. Budny, *Nuclear Fusion* **51** (8), 083001 (2011).
3. L. Frassinetti, S. Saarelma, G. Verdoolaege, M. Groth, J. C. Hillesheim, P. Bilkova, P. Bohm, M. Dunne, R. Fridström and E. Giovannozzi, *Nuclear Fusion* **61** (1), 016001 (2020).
4. P. B. Snyder, R. J. Groebner, J. W. Hughes, T. H. Osborne, M. Beurskens, A. W. Leonard, H. R. Wilson and X. Q. Xu, *Nuclear Fusion* **51** (10), 103016 (2011).
5. W. M. Tang, J. W. Connor and R. J. Hastie, *Nuclear Fusion* **20** (11), 1439 (1980).
6. F. Zonca, L. Chen and R. A. Santoro, *Plasma physics and controlled fusion* **38** (11), 2011 (1996).
7. H. R. Wilson, P. B. Snyder, G. T. A. Huysmans and R. L. Miller, *Physics of Plasmas* **9** (4), 1277-1286 (2002).
8. K. H. Burrell, T. H. Osborne, P. B. Snyder, W. P. West, M. E. Fenstermacher, R. J. Groebner, P. Gohil, A. W. Leonard and W. M. Solomon, *Physical review letters* **102** (15), 155003 (2009).
9. X. Chen, K. H. Burrell, T. H. Osborne, W. M. Solomon, K. Barada, A. M. Garofalo, R. J. Groebner, N. C. Luhmann, G. R. McKee and C. M. Muscatello, *Nuclear Fusion* **57** (2), 022007 (2016).
10. H. J. P. P. Zohm and C. Fusion, *38* (2), 105 (1996).
11. F. M. Laggner, E. Wolfrum, M. Cavedon, F. Mink, E. Viezzer, M. G. Dunne, P. Manz, H. Doerk, G. Birkenmeier and R. Fischer, *Plasma Physics and Controlled Fusion* **58** (6), 065005 (2016).
12. F. M. Laggner, A. Diallo, M. Cavedon and E. Kolemen, *Nuclear Materials and Energy* **19**, 479-486 (2019).
13. M. Kotschenreuther, D. R. Hatch, S. Mahajan, P. Valanju, L. Zheng and X. Liu, *Nuclear Fusion* **57** (6), 064001 (2017).
14. J. F. Drake, N. T. Gladd, C. S. Liu and C. L. Chang, *Physical review letters* **44** (15), 994 (1980).
15. D. R. Hatch, M. Kotschenreuther, S. Mahajan, P. Valanju, F. Jenko, D. Told, T. Görler and S. Saarelma, *Nuclear Fusion* **56** (10), 104003 (2016).
16. W. Guttenfelder, J. Candy, S. M. Kaye, W. M. Nevins, E. Wang, R. E. Bell, G. W. Hammett, B. P. LeBlanc, D. R. Mikkelsen and H. Yuh, *Physical review letters* **106** (15), 155004 (2011).
17. X. Jian, C. Holland, J. Candy, S. Ding, E. Belli, V. Chan, G. M. Staebler, A. M. Garofalo, J. McClenaghan and P. Snyder, *Physics of Plasmas* **28** (4), 042501 (2021).
18. F. Jenko, W. Dorland and G. W. Hammett, *Physics of Plasmas* **8** (9), 4096-4104 (2001).

19. J. F. Parisi, F. I. Parra, C. M. Roach, C. Giroud, W. Dorland, D. R. Hatch, M. Barnes, J. C. Hillesheim, N. Aiba and J. Ball, *Nuclear Fusion* **60** (12), 126045 (2020).
20. W. Guttenfelder, R. J. Groebner, J. M. Canik, B. A. Grierson, E. A. Belli and J. Candy, *Nuclear Fusion* **61** (5), 056005 (2021).
21. M. Kotschenreuther, X. Liu, D. R. Hatch, S. Mahajan, L. Zheng, A. Diallo, R. Groebner, J. C. Hillesheim, C. F. Maggi and C. Giroud, *Nuclear Fusion* **59** (9), 096001 (2019).
22. S. R. Haskey, A. Ashourvan, S. Banerjee, K. Barada, E. A. Belli, A. Bortolon, J. Candy, J. Chen, C. Chrystal and B. A. Grierson, *Physics of Plasmas* **29** (1), 012506 (2022).
23. D. R. Hatch, M. Kotschenreuther, S. M. Mahajan, M. J. Pueschel, C. Michoski, G. Merlo, E. Hassan, A. R. Field, L. Frassinetti and C. Giroud, *Nuclear Fusion* **61** (3), 036015 (2021).
24. D. R. Hatch, D. Told, F. Jenko, H. Doerk, M. G. Dunne, E. Wolfrum, E. Viezzer and M. J. Pueschel, *Nuclear Fusion* **55** (6), 063028 (2015).
25. D. R. Hatch, M. Kotschenreuther, S. M. Mahajan, G. Merlo, A. R. Field, C. Giroud, J. C. Hillesheim, C. F. Maggi, C. P. Von Thun and C. M. Roach, *Nuclear Fusion* **59** (8), 086056 (2019).
26. J. Chen, D. L. Brower, W. X. Ding, Z. Yan, T. Osborne, E. Strait, M. Curie, D. R. Hatch, M. Kotschenreuther and X. Jian, *Physics of Plasmas* **27** (12), 120701 (2020).
27. J. Chen, D. L. Brower, W. X. Ding, Z. Yan, M. Curie, M. Kotschenreuther, T. Osborne, E. Strait, D. R. Hatch and M. R. Halfmoon, *Physics of Plasmas* **28** (2), 022506 (2021).
28. J. Chen, W. X. Ding, D. L. Brower, D. Finkenthal and R. Boivin, *Review of Scientific Instruments* **89** (10), 10B101 (2018).
29. J. L. Luxon, *Nuclear Fusion* **42** (5), 614 (2002).
30. J. Chen, X. Jian, D. L. Brower, S. R. Haskey, Z. Yan, R. Groebner, H. Q. Wang, T. L. Rhodes, F. Laggner, W. Ding, K. Barada and S. Banerjee, *Nuclear Fusion* **63** (6), 066019 (2023).
31. R. J. Fonck, P. A. Duperrex and S. F. Paul, *Review of scientific instruments* **61** (11), 3487-3495 (1990).
32. G. R. McKee, R. J. Fonck, D. K. Gupta, D. J. Schlossberg, M. W. Shafer, R. L. Boivin and W. Solomon, *Plasma and Fusion Research* **2**, S1025-S1025 (2007).
33. J. F. Drake and Y. C. Lee, *The Physics of Fluids* **20** (8), 1341-1353 (1977).
34. J. Candy, E. A. Belli and R. V. Bravenec, *Journal of Computational Physics* **324**, 73-93 (2016).
35. X. J. J. Chen, D. L. Brower, S. R. Haskey, Z. Yan, R. Groebner, H. Q. Wang, T. L. Rhodes, F. Laggner, W. Ding, K. Barada and S. Banerjee, Submitted to *Nuclear Fusion* (2023).
36. D. R. Hatch, M. Kotschenreuther, S. Mahajan, P. Valanju and X. Liu, *Nuclear Fusion* **57** (3), 036020 (2017).
37. J. Candy and E. Belli, General Atomics Report GA-A26818, General Atomics (2010).
38. J. Candy, *Plasma Physics and Controlled Fusion* **51** (10), 105009 (2009).
39. R. Arbon, J. Candy and E. A. Belli, *Plasma Physics and Controlled Fusion* **63** (1), 012001 (2020).
40. H. Doerk, M. Dunne, F. Jenko, F. Ryter, P. A. Schneider, E. Wolfrum and A. U. Team, *Physics of Plasmas* **22** (4), 042503 (2015).
41. M. J. Pueschel, B. J. Faber, J. Citrin, C. C. Hegna, P. W. Terry and D. R. Hatch, *Physical review letters* **116** (8), 085001 (2016).
42. J. L. Larakers, M. Curie, D. R. Hatch, R. D. Hazeltine and S. M. Mahajan, *Physical Review Letters* **126** (22), 225001 (2021).
43. X. Jian, C. Holland, J. Candy, E. Belli, V. Chan, A. M. Garofalo and S. Ding, *Physical Review Letters* **123** (22), 225002 (2019).

44. J. E. Kinsey, G. M. Staebler and R. E. Waltz, *Physics of Plasmas* **15** (5), 055908 (2008).